




Diffraction of a Laguerre-Gaussian beam in Raman interaction with a spatially periodic pump field

V. G. Arkhipkin ^{1,2,*}, D. A. Ikonnikov ^{1,†} and S. A. Myslivets ^{1,2,‡}

¹*Kirensky Institute of Physics, Federal Research Center KSC SB RAS, 660036 Krasnoyarsk, Russia*

²*Department of Photonics and Laser Technology, Siberian Federal University, 660041 Krasnoyarsk, Russia*



(Received 16 December 2022; accepted 7 February 2023; published 24 February 2023)

We studied Fresnel diffraction of a Laguerre-Gaussian beam $LG_{p,l}$ with arbitrary azimuthal l and radial p indices on a grating induced during its Raman interaction with a spatially periodic pump field in an atomic medium. The diffraction pattern turned out to be more complex than the classical Talbot effect observed when a plane wave illuminates a two-dimensional grating. The simulation results show that, under certain conditions, at distances corresponding to the classical Talbot planes (integer and fractional), periodic amplitude-phase distributions appear. The diffraction patterns are not a probe-field image in the induced grating plane, but a regular array of vortex annular-shaped microbeams with an inhomogeneous intensity distribution depending on the l and p indices and with a topological charge equal to that of the initial probe beam. The intensity and spatial distribution of diffraction patterns can be controlled by Raman amplification in the induced grating by varying the pump-field intensity or the Raman detuning.

DOI: [10.1103/PhysRevA.107.023519](https://doi.org/10.1103/PhysRevA.107.023519)

I. INTRODUCTION

In recent years, the generation and study of the propagation of structured light beams [1], which have a complex amplitude and phase distribution, attracted considerable interest. Such interest is associated with their promising prospects for applications in the range from classical to quantum physics. A striking example of structured light is optical vortex fields that carry orbital angular momentum (OAM), which is conditioned by the presence of a phase singularity point, where the phase is indefinite and the field intensity is zero [2]. Vortex fields are actively studied in optics [3,4]. The study of the propagation of beams with OAM through periodic structures is of fundamental interest [5–11].

Laguerre-Gaussian (LG) beams are a wide class of optical vortex fields that carry OAM [2]. In the Cartesian coordinate system, the complex amplitude of the LG beam $LG_{p,l}$ has the following form:

$$LG_{p,l}(x, y) = 2^{l/2} \left(\frac{x + iy}{w_0} \right)^l \times \exp \left(-\frac{x^2 + y^2}{w_0^2} \right) L_p^l \left(-\frac{2(x^2 + y^2)}{w_0^2} \right), \quad (1)$$

where w_0 is the Gaussian beam waist radius, L_p^l is the associated Laguerre polynomial, l is the azimuthal index or topological charge (TC), and p is the radial index. Compared to Gaussian fields, LG ones have two additional degrees of freedom: the topological charge l and the radial index p . The

topological charge [2]

$$l = (2\pi)^{-1} \oint_C \nabla \psi(x, y) dx dy, \quad (2)$$

where $\psi(x, y)$ is the field phase, is determined by the phase singularity on the beam axis, which leads to the helical phase front shaping. The presence of a radial index leads to the formation of a set of p concentric nodal rings, each point on which is singular but has no topological charge. The shape of the intensity cross section of such beams is preserved during propagation in a homogeneous medium and has radial symmetry. These properties make LG beams useful in many applications, in particular, for free-space communication [12], quantum information processing [13], sorting [14], and orbital angular momentum imaging [15] for optical manipulations with microscopic particles [16]. Since LG beams with a large radial index have several intensity rings around the beam axis, they can therefore be used to capture several particles simultaneously in circular trajectories and make them orbit.

Although LG beams belong to the class of well-studied optical fields, they still attract the attention of researchers [17–19]. Diffraction gratings are important optical components and are used in many areas of optics. Therefore, studies of LG beams diffraction on gratings of various types are of great interest. In Ref. [20], the features of an LG laser beam Fresnel and Fraunhofer diffraction on a forked grating were theoretically studied. Gratings with varying periods are widely used to measure topological charges [21–23]. In Ref. [24], an array of tunable optical vortices was obtained by diffraction of an LG beam ($p = 0$, $l = 1$) on a two-dimensional electromagnetically induced atomic lattice under conditions of electromagnetically induced transparency. With such lattices one can dynamically control the intensity and spatial distribution of diffraction patterns; thus they are of particular interest. Optical vortex arrays with controlled

*avg@iph.krasn.ru

†ico@iph.krasn.ru

‡sam@iph.krasn.ru

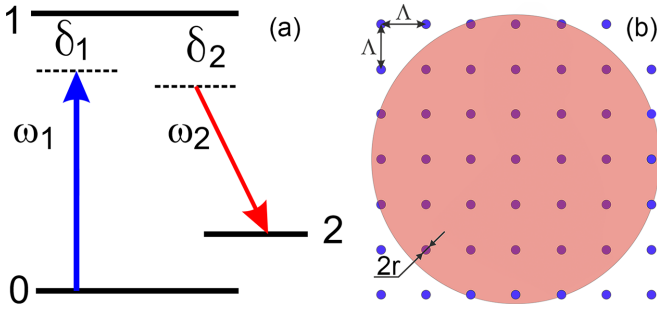


FIG. 1. (a) Configuration of energy levels of three-level atoms for Raman interaction. (b) Spatial arrangement of the pump-field microbeams with radius $r = 0.1\Lambda$ and period Λ (blue spots) and the probe LG beam (red) inside the cell with atomic gases in the x - y plane.

intensity distribution are required, for example, in multichannel optical communication and multiparticle capture applications.

In this paper, we theoretically study the diffraction patterns that arise from Fresnel diffraction of $LG_{p,l}$ beams with arbitrary azimuthal l and radial p indices under Raman interaction (stimulated Raman scattering, Raman gain) with a spatially periodic pump field in a three-level atomic Λ -system. The pump field is a two-dimensional periodic set of beams with period Λ in the x and y directions [25–27]. In the Raman interaction of a probe field with a spatially periodic pump field, an amplification and refraction grating is induced (the so-called induced Raman grating). As a result, the probe field will be diffracted by such a hybrid grating. Section II discusses the model and derives an expression for the diffracted LG field in the Fresnel approximation of the Huygens-Fresnel principle. Section III presents the results of numerical simulations of diffraction patterns under various conditions and discusses them. The main results are summarized in Sec. IV.

II. MODEL AND BASIC EQUATIONS

Let us consider the Raman gain of a probe LG field E_2 with the frequency ω_2 in the presence of a spatially modulated pump field E_1 with the frequency ω_1 in a three-level atomic medium. The energy states of a three-level Λ -system with two metastable states $|0\rangle$ and $|2\rangle$ are shown in Fig. 1(a). The frequencies of allowed transitions $|0\rangle - |1\rangle$ and $|2\rangle - |1\rangle$ are ω_{10} and ω_{12} , respectively. Only the ground state $|0\rangle$ is initially populated. The fields propagate in the z direction perpendicular to the atomic layer. The pump field is a two-dimensional periodic set of beams with radius r and period Λ in the x and y directions. The spatial arrangement of the pump beams and the probe LG beam inside the cell with atomic vapors is shown in Fig. 1(b).

When the probe field interacts with the pump, the polarization $P(\omega_2) = \chi_R(\omega_2)E_2$ is induced at the probe-field frequency ω_2 , where $\chi_R(\omega_2)$ is the Raman susceptibility and $E_2 = LG_{p,l}$ is the probe-field amplitude given by (1). The susceptibility $\chi_R(\omega_2)$ of a three-level Λ -type atomic system for the probe field can be derived by solving the density matrix equations exactly for the pump field and in the first order for the probe field (weak probe field limit $|E_2| \ll |E_1|$). In the

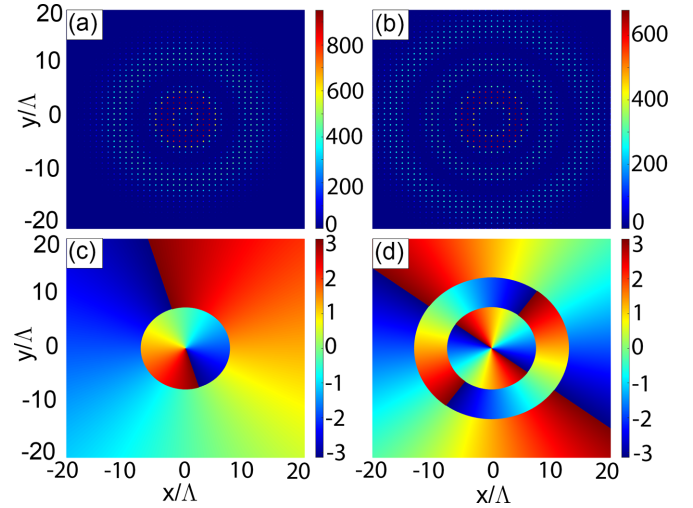


FIG. 2. Distribution of the normalized intensity (a), (b) I_2/\bar{I}_{20} and (c), (d) the phase of the probe field at the atomic medium exit. $G_1=2$, $\delta_{20} = 4$, $\omega_0 = 7.5\Lambda$. (a), (c) $l = 1$, $p = 1$ and (b), (d) $l = 2$, $p = 2$.

steady-state approximation, we have [28]

$$\chi_R(\omega_2) = \alpha_r \frac{\gamma_{12}|G_1(x, y)|^2}{\delta_1^2[\delta_{20} + i\gamma_{20} + |G_1(x, y)|^2/\delta_1]}. \quad (3)$$

Here $\alpha_r = |d_{12}|^2 N / 2\hbar\gamma_{12}$, $\delta_1 = \omega_1 - \omega_{10}$, $\delta_2 = \omega_2 - \omega_{12}$ are single-photon detunings, $\delta_{20} = \omega_1 - \omega_2 - \omega_{20}$ is the Raman (two-photon) detuning, ω_{mn} , γ_{mn} , d_{mn} are frequency, half-width and dipole matrix element of the corresponding transitions; N is atoms density, \hbar is Planck's constant. $G_1(x, y) = d_{10}E_1(x, y)/2\hbar$ is the Rabi frequency of the pump field, which represents a two-dimensional periodic function in plane x - y with period Λ in each direction. The expression (3) is derived under the condition that the pump field is detuned from state $|1\rangle$ by large one-photon detuning $\delta_1 \gg G_1$ so that single-photon absorption and the change of levels population can be neglected. For $|G_1|^2/\delta_1 > \gamma_{20}$ the ac-Stark shift of the Raman transition resonance frequency becomes noticeable. At the same time, the value of the pump-field parameters were chosen so that other nonlinear effects, such as self-focusing or self-Kerr were insignificant. A spatially periodic pump field leads to periodic modulation of the susceptibility $\chi_R(\omega_2)$ and, respectively, the Raman gain ($\text{Im } \chi_R$) and refractive index ($\text{Re } \chi_R$) for the probe field. We can say that in the process of Raman interaction, a Raman grating [28] is induced. As a result, the probe field will be diffracted by such a hybrid grating.

In the approximation when the Fresnel number is $N_f = r^2/(\lambda_2 L) \gg 1$ (r is the pump field microbeams radius, L is the atomic medium thickness, λ_2 is the probe field wavelength), the pump and probe-field microbeams' diffraction in the atomic medium volume can be ignored (thin medium approximation) [29–31]. In this case, the probe field at the atomic medium exit ($z = L$) can be represented as [32]

$$E_2(x, y, L) = T(x, y, L)E_2(x, y, z = 0),$$

where the transmission (gain) function of the medium $T(x, y, L)$ is defined as

$$T(x, y, L) = \exp[ik_2(1 + 2\pi \chi_R)L]. \quad (4)$$

It is a periodic function of the transverse coordinates x and y and depends on the Rabi frequency of the pump field and the detuning from the Raman resonance. Its value can be controlled by varying these parameters. Figure 2 shows the distributions of the intensity (scaled to the average incident probe-field intensity $\bar{I}_{20} \propto \int |E_2(z=0)|^2 dS/S$) and the phase of the probe fields at the exit from the atomic medium ($z =$

L) for some values l and p . The probe field at the atomic medium exit is amplified by Raman amplification and represents an LG beam spatially modulated by a periodic pump field.

The diffracted probe field behind the atomic medium in the near field can be calculated using the Fresnel approximation of the Huygens-Fresnel principle [30]

$$E_2(x, y, Z) = \frac{\exp(ik_2Z)}{i\lambda_2Z} \iint E_2(x_0, y_0, L) \exp\left\{\frac{ik_2}{2Z}[(x-x_0)^2 + (y-y_0)^2]\right\} dx_0 dy_0. \quad (5)$$

Here x_0, y_0 are coordinates in the grating plane $z = L$, $E_2(x_0, y_0, L) = E_{20}T(x_0, y_0, L)\text{LG}_{p,l}(x_0, y_0)$ is the probe field at the atomic medium exit and x and y are the coordinates in the observation plane $Z = z - L$. Let us expand $T(x_0, y_0, L)$ into a Fourier series as follows:

$$T(x_0, y_0, L) = \sum_{n,m} t_{nm} \exp[iG(nx_0 + my_0)], \quad (6)$$

where t_{nm} are the Fourier coefficients and $G = 2\pi/\Lambda$ is the reciprocal lattice vector modulus. Then expression (5) takes the form

$$E_2(x, y, Z) = E_{20} \frac{\exp(ik_2Z)}{i\lambda_2Z} \sum_{n,m} t_{n,m} \iint \exp\left\{\frac{ik_2}{2Z}[(x-x_0)^2 + (y-y_0)^2] + iG(nx_0 + my_0)\right\} \text{LG}_{p,l}(x_0, y_0) dx_0 dy_0. \quad (7)$$

The exponent in (7) can be converted to the form

$$\frac{ik_2}{2Z}[(x^2 - X_n^2) + (y^2 - Y_m^2)] + \frac{ik_2}{2Z}[(X_n - x_0)^2 + (Y_m - y_0)^2], \quad (8)$$

where $X_n = x - nGZ/k_2$, $Y_m = y - mGZ/k_2$.

Taking into account (8), equation (7) can be rewritten as

$$E_2(x, y, Z) = E_{20} \frac{\exp(ik_2Z)}{i\lambda_2Z} \exp\left[\frac{ik_2}{2Z}(x^2 + y^2)\right] \sum_{n,m} t_{n,m} \exp\left[-\frac{ik_2}{2Z}(X_n^2 + Y_m^2)\right] \times \iint \exp\left\{\frac{ik_2}{2Z}[(X_n - x_0)^2 + (Y_m - y_0)^2]\right\} \text{LG}_{p,l}(x_0, y_0) dx_0 dy_0. \quad (9)$$

The integral in (9) represents the Fresnel transform of the LG beam and can be calculated [3]

$$\frac{1}{i\lambda_2Z} \iint \exp\left\{\frac{ik_2}{2Z}[(X_n - x_0)^2 + (Y_m - y_0)^2]\right\} \text{LG}_{p,l}(x_0, y_0) dx_0 dy_0 = \exp[-i(2p + l + 1) \arctan(Z/z_R)] \text{LG}_{p,l}(X_n, Y_m, Z), \quad (10)$$

where

$$\text{LG}_{p,l}(X_n, Y_m, Z) = 2^{l/2} \left(\frac{X_n + iY_m}{w(Z)}\right)^l \exp\left(-\frac{X_n^2 + Y_m^2}{q^2(Z)}\right) L_p^l\left(-\frac{2(X_n^2 + Y_m^2)}{w^2(Z)}\right),$$

$1/q^2(Z) = 1/w^2(Z) - ik_2/2R(Z)$ is the complex parameter of the Gaussian beam, $w(Z) = w_0(1 + Z^2/z_R^2)^{1/2}$, $R(Z) = Z(1 + z_R^2/Z^2)$, $z_R = k_2w_0^2/2$.

As a result, the field E_2 at a distance Z from the grating can be represented as a superposition of the spatial harmonics

$$E_2(x, y, Z) = E_{20} \frac{w_0}{w(Z)} \exp\left[ik_2Z + \frac{ik_2}{2Z}(x^2 + y^2) - i(2p + l + 1) \arctan(Z/z_R)\right] \sum_{n,m} t_{nm} \exp\left[-\frac{ik_2}{2Z}(X_n^2 + Y_m^2)\right] \text{LG}_{p,l}(X_n, Y_m, Z). \quad (11)$$

The phase term in summation can be conveniently rewritten as

$$-\frac{ik_2}{2Z}(X_n^2 + Y_m^2) = -\frac{ik_2}{2Z}(x^2 + y^2) + iG(xn + ym) - \frac{i2\pi\lambda_2Z}{2\Lambda^2}(n^2 + m^2). \quad (12)$$

One can see that the spatial harmonic phase dependence on the longitudinal coordinate Z is determined by the last term in the expression (12). It is easy to show that at distances multiple of $Z_T = 2\Lambda^2/\lambda_2$, all spatial harmonics acquire the same phase shift multiple of 2π , and therefore, a regular diffraction pattern will form in these planes with a period equal to the period of the original gratings. This expression exactly coincides with the classical expression for the Talbot length in the case of the plane

waves' near-field diffraction [33,34]. Finally, the expression for the E_2 field is

$$E_2(x, y, Z) = E_{20} \frac{w_0}{w(Z)} \exp[ik_2 Z - i(2p + l + 1) \arctan(Z/z_R)] \times \sum_{n,m} t_{nm} \exp[iG(xn + ym)] \exp\left[-i2\pi(n^2 + m^2) \frac{Z}{Z_T}\right] LG_{p,l}(X_n, Y_m, Z). \quad (13)$$

This shows that the diffracted probe field in the near field is a superposition of spatial harmonics, each of which is an LG beam. For $l \neq 0$, each harmonic has a singular point where topological charge is equal to that of the incident beam. The position of the singular point is determined by the conditions $X_n = x - nGZ/k_2 = 0$, $Y_m = y - mGZ/k_2 = 0$. It can be seen that each harmonic propagates in the direction of the corresponding diffraction order $x/Z = n\lambda_2/\Lambda$, $y/Z = m\lambda_2/\Lambda$. At a distance $Z = Z_T$, these relations take the form $x/\Lambda = 2n\Lambda$ and $y/\Lambda = 2m\Lambda$, that is, in this plane, all harmonics are centered at even values of Λ . However, the resulting diffraction pattern is determined by the interference of all harmonics and the position of singularities may not coincide with those for individual harmonics. For $l = 0$, $p = 0$, the probe wave is a Gaussian beam and has no TC (it is not a vortex). The diffraction patterns in the Talbot planes have the same form as in the classical Talbot effect.

III. RESULTS AND DISCUSSION

In numerical calculations, parameters corresponding to the D1 line of sodium atoms were used. Metastable levels $|0\rangle$ and $|2\rangle$ correspond to long-lived sublevels of the ground state $^2S_{1/2}$. The parameters of this atomic system can be given by $\gamma_{10}/2\pi = 10$ MHz, $\gamma_{21} = \gamma_{10}$, $\gamma_{20} = \gamma_{10}/100$. The Rabi frequency G_1 and one-photon detuning δ_1 are given in the γ_{10} units, the Raman detuning δ_{20} in the γ_{20} units: $G_1 = 2$, $\delta_1 = -100$, $\delta_{20} = 4$. The Raman detuning value was chosen to compensate for the ac-Stark shift and ensure resonant conversion conditions. The atomic media length $L = 75 \mu\text{m}$. The grating period is $\Lambda = 600\lambda_2$, $w_0 = 7.5\Lambda$, $r = 0.1\Lambda$.

Figure 3 shows diffraction patterns in different Talbot planes. In integer Talbot planes [Figs. 3(a) and 3(b)], complex periodic amplitude distributions are observed, which differ from the field self-images on the grating [Fig. 2(a)]. The central microbeam has an annular intensity distribution while microbeams not lying in the center of symmetry acquire a crescent-shaped distribution and are rotated at a certain angle relative to the center of the diffraction pattern, depending on their coordinates. It can be seen from the figure that the formed microbeams are not LG beams and the diffraction pattern is not a self-image of the field on the grating. It turns out to be more complicated than the classical Talbot effect observed where the grating is illuminated by a plane wave. But it can be considered as an analog of the Talbot effect (quasi-Talbot effect). Similar diffraction patterns are also observed in other, including fractional, Talbot planes. Figures 3(c) and 3(d) show the diffraction patterns in the fractional Talbot planes $Z = 1/2Z_T$ and $Z = 1/4Z_T$. It can be seen that, as in the classical Talbot effect, in the $Z = 1/2Z_T$ plane, microbeams are formed in positions shifted by half a

period along both axes in the transverse plane and in the $Z = 1/4Z_T$ plane the period of the diffraction pattern is halved. Although on the Talbot length all harmonics acquire the same phase shift multiple of 2π , nevertheless, due to the curvature of the wavefront of the original beam and, accordingly, the individual harmonics, the diffraction patterns in different Talbot planes will differ from each other: with increasing coordinate Z , the transverse dimensions of the microbeams will increase; moreover, the intensity distribution within the microbeams themselves will change, but their position will remain unchanged and is determined by the grating period. With a further increase in the coordinate $Z > 2Z_T$ (for the given parameters), the microbeams begin to overlap significantly, as a result, the diffraction pattern becomes more complicated.

Obviously, the diffraction pattern depends on the choice of the parameters of the interacting fields and is determined by their ratio. Figure 4 shows intensity distributions of the central microbeam in the $y = 0$ plane in diffraction patterns depending on the chosen parameters r , w_0 , l , and p . As expected, the increasing of the pump beams' radius r leads to an increase of the microbeam relative intensity [Fig. 4(a)]. One can see that for r less than a certain value, the intensity distribution has a set of low-intensity rings and their quantity is equal to the radial index p of the incident LG beam. If this value is exceeded, the number of low-intensity rings decreases by 1. An increase in the waist radius leads to a decrease in the wavefront curvature of the incident LG beam and, accordingly, to a decrease in the microbeam diameter [Fig. 4(b)].

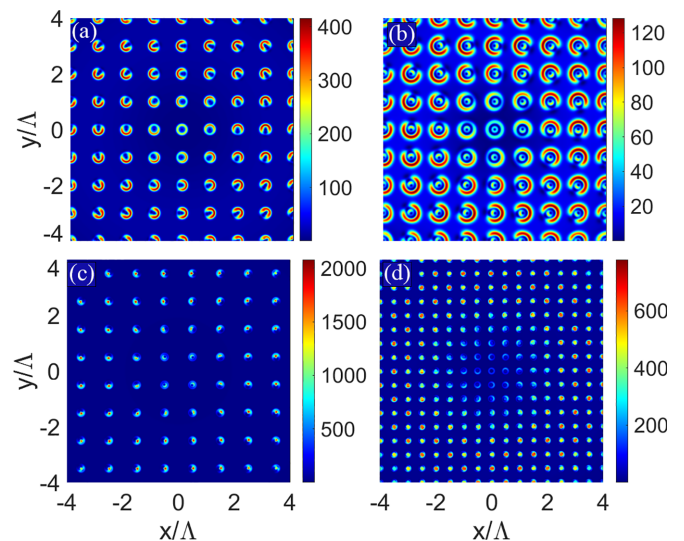


FIG. 3. Intensity distribution of diffraction patterns for an LG probe field with $l = 1$, $p = 1$ at the distance (a) $Z = Z_T$, (b) $Z = 2Z_T$, (c) $Z = 0.5Z_T$, and (d) $Z = 0.25Z_T$.

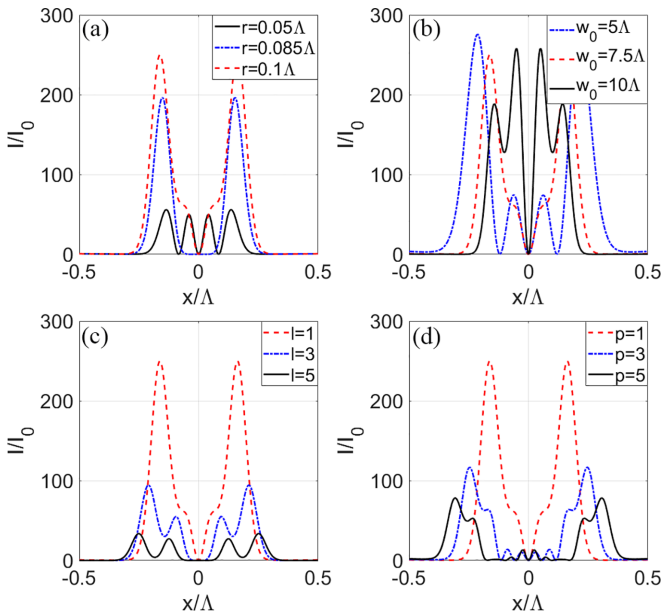


FIG. 4. Intensity distributions of the central microbeam at $y = 0$ in diffraction patterns at a distance $Z = Z_T$ depending on the chosen parameters: (a) $w_0 = 7.5\Lambda$, $l = 1$, $p = 1$; (b) $r = 0.1\Lambda$, $l = 1$, $p = 1$; (c) $r = 0.1\Lambda$, $w_0 = 7.5\Lambda$, $p = 1$; and (d) $r = 0.1\Lambda$, $w_0 = 7.5\Lambda$, $l = 1$.

Increasing the topological charge l and/or the radial number p of the incident LG beam leads to the microbeam broadening [Figs. 4(c) and 4(d)] with a decrease in its amplitude. Also, a change in p leads to a corresponding change in the number of low-intensity rings in the microbeam.

In addition, the diffraction pattern depends on the transmission function $T(x, y)$ defined by Eq. (4), and can be controlled by varying the Rabi frequency of the pump field G_1 and the detuning from the Raman resonance δ_{20} . Figure 5 shows the

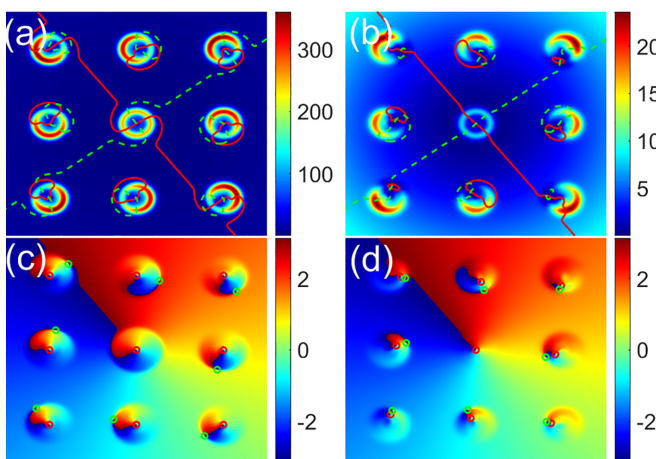


FIG. 5. (a), (b) Intensity and (c), (d) phase distribution of diffracted field at different values of the Rabi frequency of the pump field in the $Z = Z_T$ plane, $l = 1$ and $p = 1$: (a), (c) $G_1 = 2$, (b), (d) $G_1 = 1.7$. Solid (red) and dashed (green) lines are the zero isolines of the imaginary and real parts of the diffracted field, respectively. Green and red circles mark the position of singularities with negative and positive TC, respectively.

diffraction patterns for various values of the Rabi frequency of the pump field. The singularities' position (green and red circles) are found as intersection points of isolines with zero values of the imaginary and real parts of the diffracted field (solid red and dashed green lines). The value and sign of the singularity's TC are calculated by Eq. (2). For $G_1 = 1.7$ the amplification is significantly less, thus, the contribution from the parts of the incident field that have passed without amplification becomes more significant. As a result, it can be seen that, in this case, the shape of the incident beam is more clearly manifested in the diffraction pattern; in addition, the position of the singular points changes.

Figure 6 shows diffraction patterns in the $Z = Z_T$ plane for different values of the l and p parameters. The second and third rows show the intensity and phase distribution in the central microbeam. The two bottom rows show the intensity and phase distribution in the lateral microbeam (corresponding to the pink squares from the top row). The analysis shows that, although the microbeams contain rings with a much lower intensity, these rings are not nodal since the intersection of the zeros of the imaginary (solid red line) and real (dashed green line) parts of the field occurs only in certain points. The total number of singular points depends on l and p indices. Note that diffraction patterns have a fine structure, i.e., each of the vortex microbeams consists of several spatially overlapping vortices, some of which rotate clockwise and some counterclockwise. For $l \neq 0$, all microbeams have a TC equal to the charge of the original LG beam. There are also vortices localized in the low-intensity region near the lateral microbeams. Their total charge is opposite in sign and compensates for the charge of the vortices located inside the lateral microbeams. The central microbeam reproduces l of the initial LG field. Therefore, the total TC of the entire diffracted field also coincides with that of the probe field.

Figure 7 shows overview distributions of the diffracted field intensity and phase for various values of l and p in the $Z = Z_T$ plane. In the LG beam with a radial index $p \neq 0$, there is a set of concentric circles with zero intensity at the boundary of which a phase jump occurs. The number of circles is equal to the value of the radial index p . From the examination of the entire set of microbeams formed by diffraction of such an LG beam (Fig. 7), then one can see that the spatial intensity and phase distribution of the diffraction pattern as a whole reflects that of the original LG beam (see Fig. 2). However, where the circle-shaped phase discontinuity is crossed by microbeams, the phase distribution is distorted and the shape of the circle is violated. It can be seen that, when going around the singular point at the center of the diffraction pattern, the phase changes by $2\pi l$ (as in an ordinary vortex). Thus, although the total diffracted field is also a vortex and its phase during propagation rotates around the optical axis with a TC equal to that of the probe field, it cannot be called an LG beam.

It should be noted that since expression (13) was obtained in the Fresnel approximation (i.e., it includes but is not limited to the terms used in the Fraunhofer approximation [35]), thus it can also calculate the diffraction pattern in the far field ($Z \gg z_R$). The diffracted field still will be a superposition of spatial harmonics, but in this case, they will no longer be overlapping in space. Thus, the diffraction pattern in the far field will be a set of LG beams propagating at angles corresponding

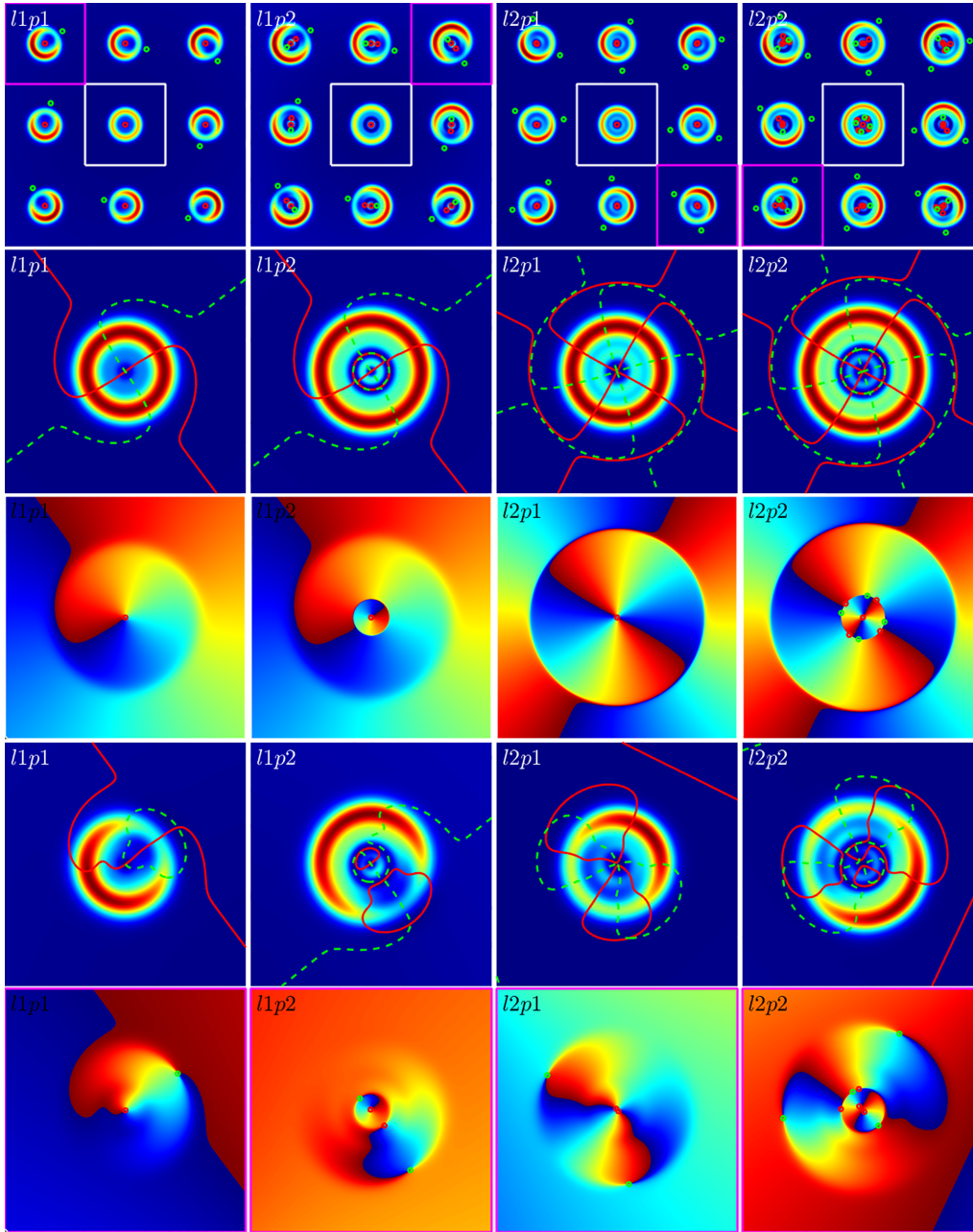


FIG. 6. Diffraction patterns in the $Z = Z_r$ plane for different values of the l and p parameters (top row). Next two rows show the intensity and phase distribution in the central microbeam; two bottom row shows the intensity and phase distribution in the side microbeam (corresponding to the pink squares from the top row). Solid (red) and dashed (green) lines are the zero isolines of the imaginary and real parts of the diffracted field, respectively.

to the diffraction-order directions $\{x, y\}/Z = \{n, m\}\lambda/\Lambda$, with the same l and p indices as the original beam. Figure 8 shows distributions of the diffracted field intensity and phase in the far field for the central beam. During the propagation, the phase quickly rotates and in the far field a large number of spiral turns are present inside the beam. Nodal rings (black dotted lines) intersect this phase spiral, the number of rings being equal to radial index p . The corresponding distributions in the lateral beams in planes normal to their respective direction of propagation will be exactly the same. The presence of phase singularity in the center and the set of nodal rings

confirms that each beam in the far field represents the LG beam.

IV. CONCLUSION

The diffraction of LG beams ($p \neq 0, l \neq 0$) in the Raman interaction with a spatially periodic pump field is studied theoretically. It is shown that the diffracted field in the near zone is a superposition of spatial harmonics, which are an LG beam. At distances corresponding to the classical Talbot lengths in the transverse plane, regular spatial structures with

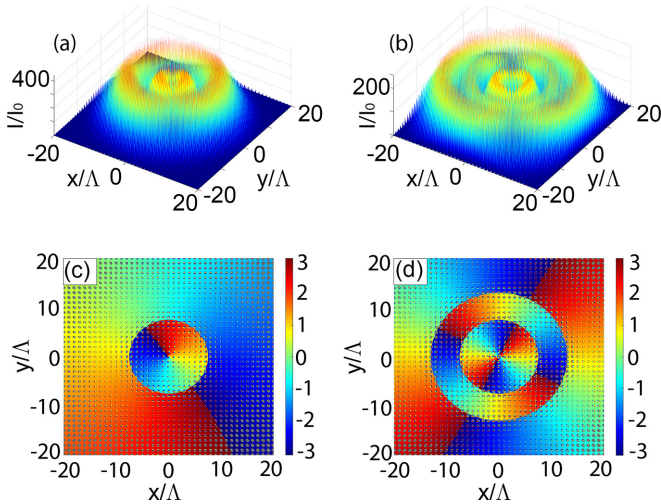


FIG. 7. (a), (b) Intensity and (c), (d) phase distributions of the diffraction field at a distance $Z = Z_T$. (a), (c) $l = 1$, $p = 1$, (b), (d) $l = 2$, $p = 2$.

the period of the induced grating are observed. They differ from the self-images of the probe field on the induced grating exit and are periodic arrays of microbeams with a nonuniform intensity distribution. The diffraction pattern can be considered as an analog of the classical Talbot effect. Despite the fact that microbeams contain low-intensity rings at $p \neq 0$, nevertheless, only individual points in these rings are zero crossings of the real and imaginary parts of the field and, accordingly, microbeams are not LG beams. All microbeams have a TC equal to the charge of the original probe beam. However, near each beam (except the central one) there are singularities of the opposite sign, so their effective charges are equal to zero. Therefore, the TC of the entire diffracted field also coincides with the probe-field charge and the total diffracted field is a vortex. The spatial distribution of the diffracted field

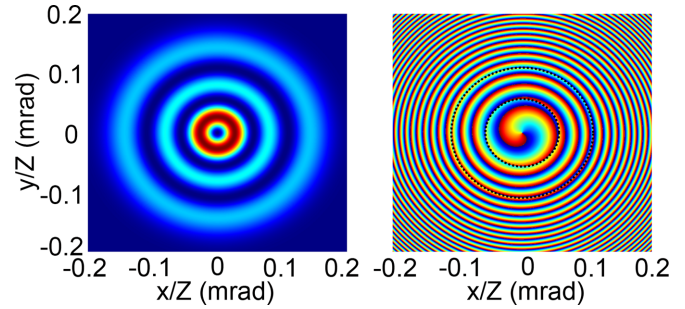


FIG. 8. Intensity and phase distributions of the diffraction in the far field ($Z = 10z_R$), $l = 1$, $p = 2$ for the central beam; black dotted line shows positions of nodal rings.

corresponds to the structure of the incident LG beam, but the annular discontinuities of the phase caused by the radial index p are distorted in those places where these rings are crossed by microbeams. In the far field, the diffraction patterns are also a superposition of harmonics, but unlike the near-field zone, they do not overlap in space. That is why the diffraction patterns in the far field represent a set of LG beams with the same l and p indices as the original beam. The intensity of diffraction images can be controlled by Raman gain in the induced grating by varying the pump-field intensity or the Raman detuning. The results may be promising for the realization of fundamental light-matter interactions. Vortex beams with controlled intensity and spatial distribution may be of interest for simultaneous optical trapping and manipulations of multiple particles, for high-density multichannel quantum communications, and for cryptography.

ACKNOWLEDGMENT

This work was supported by the Russian Science Foundation (Grant No. 19-12-00203).

- [1] A. Forbes, M. de Oliveira, and M. R. Dennis, Structured light, *Nat. Photon.* **15**, 253 (2021).
- [2] G. J. Gbur, *Singular Optics* (CRC Press, Boca Raton, FL, 2017).
- [3] V. V. Kotlyar, A. A. Kovalev, and A. P. Porfirev, *Vortex Laser Beams* (CRC Press, London, 2018).
- [4] Y. Shen, X. Wang, Z. Xie, C. Min, X. Fu, Q. Liu, M. Gong, and X. Yuan, Optical vortices 30 years on: OAM manipulation from topological charge to multiple singularities, *Light Sci. Appl.* **8**, 90 (2019).
- [5] B. Knyazev, O. Kameshkov, N. Vinokurov, V. Cherkassky, Y. Choporova, and V. Pavelyev, Quasi-Talbot effect with vortex beams and formation of vortex beamlet arrays, *Opt. Express* **26**, 14174 (2018).
- [6] W. Zhang, J. Tang, P. Chen, G. Cui, Y. Ming, W. Hu, and Y. Lu, Evolution of orbital angular momentum in a soft quasi-periodic structure with topological defects, *Opt. Express* **27**, 21667 (2019).
- [7] S. Rasouli and D. Hebri, Theory of diffraction of vortex beams from 2d orthogonal periodic structures and Talbot self-healing under vortex beam illumination, *J. Opt. Soc. Am. A* **36**, 800 (2019).
- [8] I. A. Kotelnikov, O. E. Kameshkov, and B. A. Knyazev, Diffraction of Bessel beams on 2d amplitude gratings—a new branch in the Talbot effect study, *J. Opt.* **22**, 065603 (2020).
- [9] P. Amiri, A. M. Dezfouli, and S. Rasouli, Efficient characterization of optical vortices via diffraction from parabolic-line linear gratings, *J. Opt. Soc. Am. B* **37**, 2668 (2020).
- [10] D. A. Ikonnikov, S. A. Myslivets, M. N. Volochaev, V. G. Arkhipkin, and A. M. Vyunishev, Two-dimensional Talbot effect of the optical vortices and their spatial evolution, *Sci. Rep.* **10**, 20315 (2020).
- [11] V. G. Arkhipkin and S. A. Myslivets, Diffraction of vortex Gaussian beams from a two-dimensional Raman-induced grating, *Laser Phys.* **31**, 065401 (2021).
- [12] G. Gibson, J. Courtial, M. J. Padgett, M. Vasnetsov, V. Pas'ko, S. M. Barnett, and S. Franke-Arnold, Free-space information transfer using light beams carrying orbital angular momentum, *Opt. Express* **12**, 5448 (2004).
- [13] A. Mair, A. Vaziri, G. Weihs, and A. Zeilinger, Entanglement of the orbital angular momentum states of photons, *Nature (London)* **412**, 313 (2001).

- [14] H. Wei, X. Xue, J. Leach, M. J. Padgett, S. M. Barnett, S. Franke-Arnold, E. Yao, and J. Courtial, Simplified measurement of the orbital angular momentum of single photons, *Opt. Commun.* **223**, 117 (2003).
- [15] L. Torner, J. P. Torres, and S. Carrasco, Digital spiral imaging, *Opt. Express* **13**, 873 (2005).
- [16] L. Paterson, M. P. MacDonald, J. Arlt, W. Sibbett, P. E. Bryant, and K. Dholakia, Controlled rotation of optically trapped microscopic particles, *Science* **292**, 912 (2001).
- [17] V. Kotlyar, A. Kovalev, and A. Savelyeva, Topological charge of a superposition of identical parallel single-ringed Laguerre-Gaussian beams, *Computer Optics* **46**, 184 (2022).
- [18] M. G. G. Abad and M. Mahmoudi, Laguerre-Gaussian modes generated vector beam via nonlinear magneto-optical rotation, *Sci. Rep.* **11**, 5972 (2021).
- [19] Y. Yang, Y. Li, and C. Wang, Generation and expansion of Laguerre-Gaussian beams, *J. Opt.* **51**, 910 (2022).
- [20] S. Topuzoski, Fresnel and Fraunhofer diffraction of (l, n) -th mode Laguerre-Gaussian laser beam by a fork-shaped grating, *J. Mod. Opt.* **66**, 1514 (2019).
- [21] K. Dai, C. Gao, L. Zhong, Q. Na, and Q. Wang, Measuring oam states of light beams with gradually-changing-period gratings, *Opt. Lett.* **40**, 562 (2015).
- [22] S. Zheng and J. Wang, Measuring orbital angular momentum (oam) states of vortex beams with annular gratings, *Sci. Rep.* **7**, 40781 (2017).
- [23] S. Rasouli, S. Fathollahzade, and P. Amiri, Simple, efficient and reliable characterization of Laguerre-Gaussian beams with non-zero radial indices in diffraction from an amplitude parabolic-line linear grating, *Opt. Express* **29**, 29661 (2021).
- [24] J. Yuan, H. Zhang, C. Wu, L. Wang, L. Xiao, and S. Jia, Tunable optical vortex array in a two-dimensional electromagnetically induced atomic lattice, *Opt. Lett.* **46**, 4184 (2021).
- [25] U. Krackhardt and N. Streibl, Design of dammann-gratings for array generation, *Opt. Commun.* **74**, 31 (1989).
- [26] N. Streibl, Beam shaping with optical array generators, *J. Mod. Opt.* **36**, 1559 (1989).
- [27] S. Ning, J. Lu, S. Liang, Y. Feng, C. Li, Z. Zhang, and Y. Zhang, Talbot effect of an electromagnetically induced square photonic lattice assisted by a spatial light modulator, *Opt. Lett.* **46**, 5035 (2021).
- [28] V. G. Arkhipkin and S. A. Myslivets, One- and two-dimensional Raman-induced diffraction gratings in atomic media, *Phys. Rev. A* **98**, 013838 (2018).
- [29] S. Akhmanov and S. Nikitin, *Physical Optics* (Clarendon Press, New York, 1997).
- [30] J. Goodman, *Introduction to Fourier Optics*, McGraw-Hill Physical and Quantum Electronics Series (W. H. Freeman, New York, 2005).
- [31] L. Zhao, W. Duan, and S. F. Yelin, All-optical beam control with high speed using image-induced blazed gratings in coherent media, *Phys. Rev. A* **82**, 013809 (2010).
- [32] N. B. Delone and V. P. Krainov, *Fundamentals of Nonlinear Optics of Atomic Gases*, Pure & Applied Optics (John Wiley & Sons, Nashville, TN, 1988).
- [33] K. Patorski, *The Self-Imaging Phenomenon and its Applications* (Elsevier, Amsterdam, 1989), pp. 1–108.
- [34] J. Wen, Y. Zhang, and M. Xiao, The Talbot effect: recent advances in classical optics, nonlinear optics, and quantum optics, *Adv. Opt. Photon.* **5**, 83 (2013).
- [35] K. Iizuka, in *Engineering Optics*, 3rd ed. (Springer, New York, 2008), p. 532.